3.1 Introduction

Ruddlesdon Popper (RP) phase has the chemical formula $A_{n+1}B_nO_{3n+1}$; where n is an integer, for example, n=1 corresponds to A_2BO_4 etc. [168]. The A_2BO_4 structure consists stacking of perovskite (ABO_3) and rock salt (AO) layer alternating along c-axis. A_2BO_4 based mixed ionic-electronic conductors (MIECs) have received interest due to their high thermal stability, high oxygen diffusion coefficient, excellent electronic conductivity and strong electrocatalytic activity towards Oxygen Reduction Reaction (ORR) [169]. Mixed oxide ion and electron conducting ceramic materials $A_2BO_{4+\delta}$ (Where, A = La^{3+}, Nd^{3+} or Pr^{3+} and B = $Cu^{2+/3+}$, $Ni^{2+/3+}$ or $Co^{2+/3+}$) have attracted attention for cathode of intermediate-temperature solid oxide fuel cell (IT-SOFC), ceramic membranes for oxygen separation as well as applications involving partial oxidation of light hydrocarbons [170]. The oxygen stoichiometry in $La_2NiO_{4+\delta}$ compounds have been controlled either by partial substitution of alkaline earth (Sr, Ba, Ca) at La site or transition metals (Cu and Co) at Ni site [171]. During the last decade alkaline earth orthostannates, M_2SnO_4 (M: Ca, Sr, Ba) have been used as host for new phosphors materials because of their stable crystalline structure, high physical and chemical stability and wide band gap [172].

Ruddlesdon Popper (RP) strontium orthostannate (Sr_2SnO_4) oxide has tetragonal structure with space group I4/mmm like K_2NiF_4. The lattice parameters of Sr_2SnO_4 oxide is a=b= 4.052 Å and c= 12.581 Å [173]. Rare earth elements (Eu, Sm, Nd, Tb, Dy) doped Sr_2SnO_4 materials have exhibited interesting emission properties [174]. On the other hand, terbium (Tb) doped strontium orthostannates system has been reported as yellow pigments with high infrared reflectance coefficient which can be used for energy saving applications [175]. To the best of our knowledge, no report is available in the literature on dielectric and AC electrical conduction behaviour of Sr_2SnO_4. Therefore, it is considered worthwhile to synthesize this material and study its dielectric and electrical properties in wide range of

temperature and frequency. These studies will definitely enhance basic knowledge of solid state physics which is essential for exploring applications of Sr_2SnO_4.

3.2 Results and Discussions:

3.2.1 Study of reaction mechanism using TGA/DSC and XRD

The thermogravimetric (TGA) and differential scanning calorimetric (DSC) curves of SnO_2 and $SrCO_3$ powders recorded after grinding it for 1 hr in an agate mortar with pestle are shown in Figures 3.1(a) and (b), respectively. No significant changes were observed in TGA/DSC curve of SnO_2 in the temperature range 30–1000 °C, however the TGA curve of $SrCO_3$ (as shown in Figure 3.1 (b)) shows a single step weight loss (approximately 27.58 %) in the temperature range 850–1000°C. Theoretically, decomposition of $SrCO_3$ takes place according to the reaction given by Eq. (1);

$$SrCO_3 \rightarrow SrO + CO_2 \qquad (3.1)$$

Weight loss calculated according to Eq. (3.1) is 29.72 % which is slightly higher than the observed experimental weight loss (27.58 %). These results suggest that $SrCO_3$ has not been completely decomposed into SrO within the investigated temperature range due to use of higher heating rate (10^oC/min) in instrument. Two endothermic reaction peaks centered at 926 °C and 977 °C are seen in the DSC curve of $SrCO_3$ is in agreement with results report by J. Bera et al. [176]. The first peak is assigned to the polymorphic phase transformation of $SrCO_3$ from orthorhombic (space group $Pmcn$) to rhombohedral (space group $R\bar{3}m$) while the second peak to the decomposition of $SrCO_3$ into SrO according to reaction (3.1) [176].

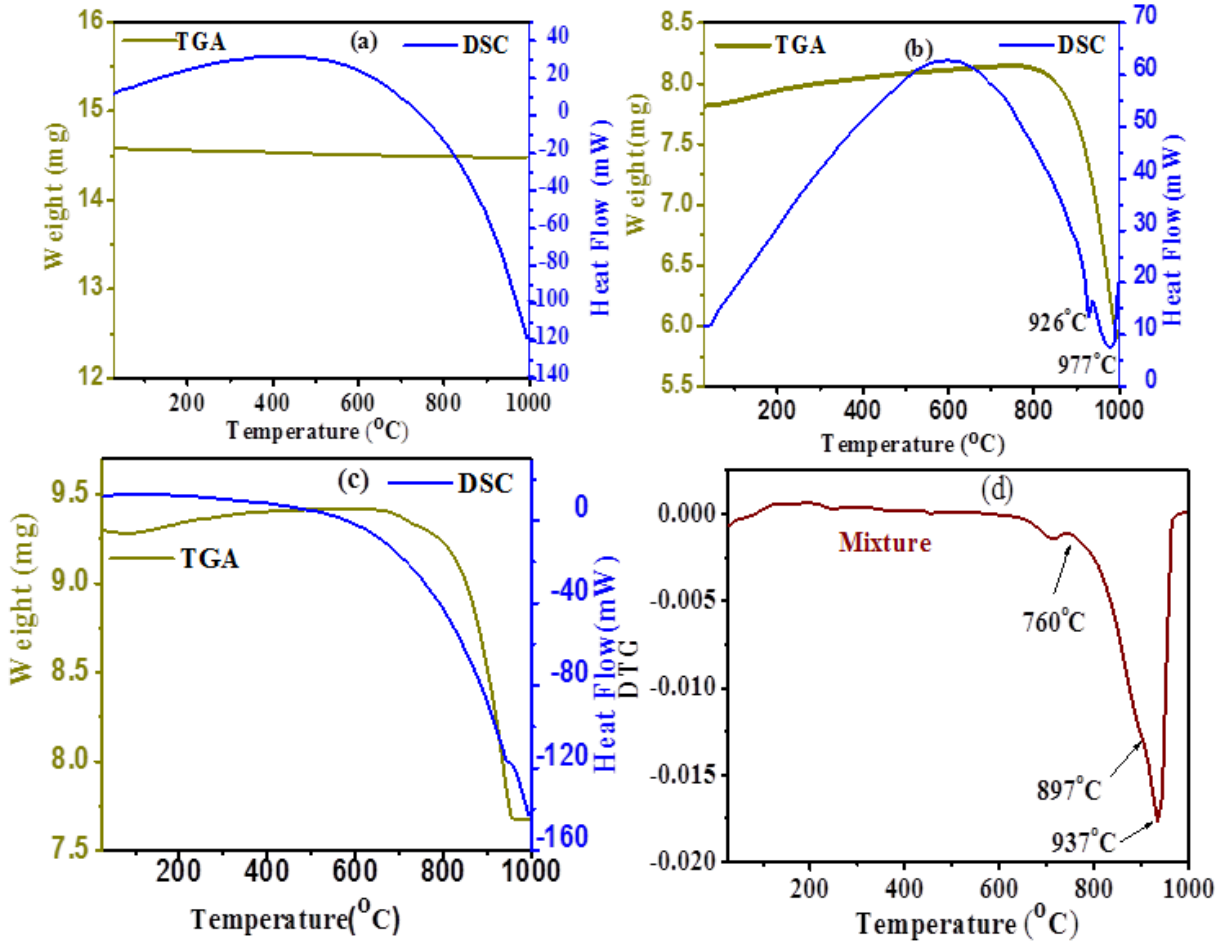

Figure 3.1 Simultaneous TGA/DSC curve of (a) raw material SnO_2 (b) raw material $SrCO_3$ (c) mixture of raw material $SrCO_3$ and SnO_2 (d) Derivative of thermogravimetric (DTG) curve of a mixture of raw materials.

Figure 3.1(c) shows the TGA/DSC curves of the stoichiometric mixture of raw materials (2 mole $SrCO_3$ and 1 mole SnO_2) obtained after ball milling for the formation of Sr_2SnO_4. The TGA curve shows a weight loss of approximately 19.1% in the temperature range of 650-950°C. In order to have a more clear visualization of weight loss steps occurring in the mixture, dm/dT vs. temperature, i.e., derivative thermo-gravimetric (DTG) plot has been generated from its TG data and illustrated in Figure 3.1(d). The DTG curve depicts two distinct peaks in the temperature range 650-750°C, and 800-950°C and weight losses corresponding to these peaks were found to be 1.06 % and 17.04 %. It is expected that

reaction between raw materials ($SrCO_3$ and SnO_2) for the formation of Sr_2SnO_4 will take place according to reaction given by Eq. (3.2);

$$2SrCO_3 + SnO_2 \rightarrow Sr_2SnO_4 + 2CO_2 \quad (3.2)$$

The weight loss calculated theoretically according to Eq. (3.2) is 19.7% which is approximately equal to the sum of the weight losses observed experimentally in two different temperature ranges mentioned above. This result confirms that the decomposition of the $SrCO_3$ into SrO has taken place below 950^oC which is slightly lower than the decomposition temperature observed for raw $SrCO_3$ (Figure 3.1(b)). In the DSC curve of the mixture, a weak endothermic peak around 942^oC was found which may be assigned to the formation of Sr_2SnO_4. The observed lower decomposition temperature and absence of a peak in DSC curve corresponding to change in the crystal structure of $SrCO_3$ in the mixture is possible on account of prolonging ball milling (8 h). During ball milling, particle size of the reactants get reduced which possibly results a change in the crystal structure. Considering that the major amount of decomposition of $SrCO_3$ into SrO and CO_2 in the mixture occurred at a temperature higher than 800$^{\circ}C$ (Figure 3.1(c) and (d)), thus the calcination of the mixture was carried out at three different temperatures 800^oC, 900^oC and 1000^oC for 8 h to understand reaction steps involved in the formation of Sr_2SnO_4.

In order to understand the complete reaction mechanism, powder X-ray diffraction technique has been used. The X-ray diffraction pattern of the powders obtained after calcination is illustrated in Figure 3.2. These patterns were compared with standard XRD profile available for $SrCO_3$(COD-1539128), SrO [177], SnO_2(COD-1000062) , $SrSnO_3$ (COD-1521093) and Sr_2SnO_4 (COD-1539931) compounds. X-ray diffraction pattern of the powder obtained after calcination at 800^oC contains peaks mainly of raw materials $SrCO_3$ and SnO_2 along with a small intensity peak (at 31.44^o) of $SrSnO_3$ phase. No peak of Sr_2SnO_4

phase was found in the XRD pattern. The formation of a small amount of $SrSnO_3$ may occur due to a direct reaction between $SrCO_3$ and SnO_2 according to the following reaction;

$$SrCO_3 + SnO_2 \rightarrow SrSnO_3 + CO_2 \quad (3.3)$$

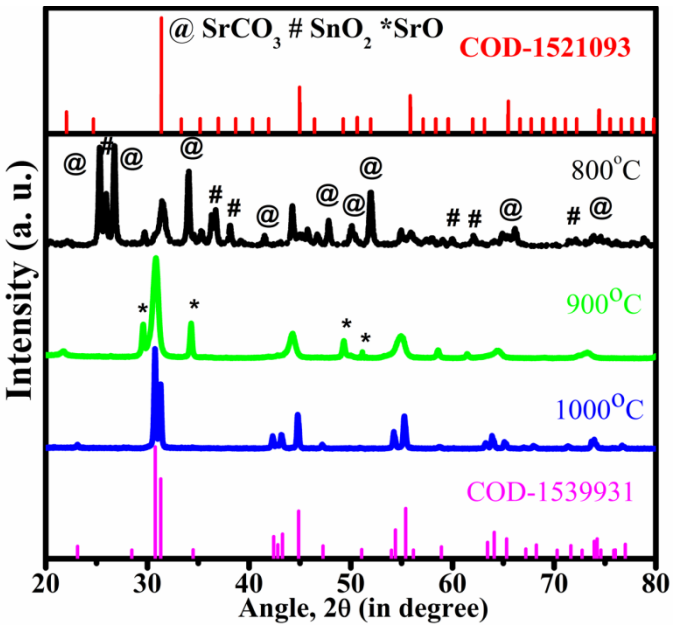

Figure 3.2 Powder X-ray diffraction pattern of the prepared mixture calcined at different temperatures.

This result is in agreement with the DTG results which exhibited a small weight loss in the temperature range below 800°C. However, the XRD clearly indicated that the major amount of reactant $SrCO_3$ has not decomposed into SrO. As the calcination temperature increased from 800 to 900°C, peaks corresponding to the SnO_2 and $SrCO_3$ phases disappeared. Furthermore, the intensity of peaks corresponding to $SrSnO_3$ phase gradually increased and few peaks of SrO phase is appeared in the XRD pattern. The XRD pattern of the powder calcined at 1000°C contains only peaks belongs to Sr_2SnO_4 phase. Therefore, XRD result confirms that the endothermic peak in the DSC (Figure 3.1(c)) curve is due to reaction of SrO and $SrSnO_3$ for the formation of Sr_2SnO_4 according to following reaction:

$$SrO + SrSnO_3 \rightarrow Sr_2SnO_4 \quad (3.4)$$

On the basis of detailed thermal analysis (Figure 3.1(a), (b), (c) and (d)) combined with the XRD (Figure 3.2), the formation mechanism of Sr_2SnO_4 from the mixture of $2SrCO_3$-SnO_2 is schematically illustrated by **Core-Shell model** as shown in Figure 3.3.

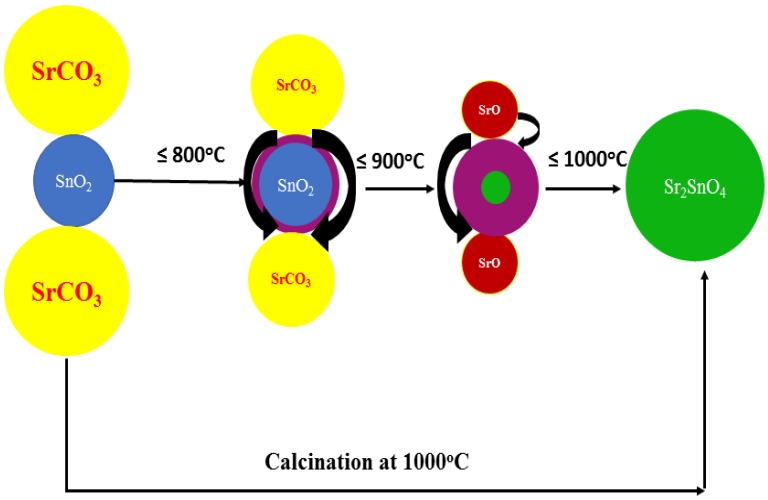

Figure 3.3 Core-shell model for the phase formation of Sr_2SnO_4 using raw materials $SrCO_3$ and SnO_2.

3.2.2 Phase Formation and Structural Characterization using XRD

To determine various structural parameters such as lattice parameters, unit cell volume, theoretical density, bond length, bond angle, Rietveld refinement of XRD pattern of phase pure powder has been performed. The Rietveld refinement of the X-ray diffraction pattern was carried out using '**FullProf Software Suite**'. For the refinement, structure of Sr_2SnO_4 oxide is considered as tetragonal and space group I4/mmm. The pseudo-voight function is adopted for the peak shape, while the background is described by the interpolation between a set of background points with refineable heights. The scale factor, zero correction, background, half-width parameters, lattice parameters (a, b, c), angle (α, β, γ), positional coordinate (x, y, z) and the thermal parameters (B) are varied during the process of refinement while the occupancy parameters for all the ions kept fix. After the repetition of refinement the XRD pattern is obtained and shown in Figure 3.4. The value of structural

parameters such as lattice parameter, unit cell volume, bond lengths, bond angles, and other relevant parameters obtained from the refinement are presented in Table 3.1. Final value of the fitting parameters R_p, R_{wp}, $R_{f,}$ and χ^2 are given in Table 3.1. The value of goodness of fit ($S = R_{wp}/R_p$) parameter lies between 1.02 – 1.22 reasonable for assigning the structure A_2BO_4 [178].

The structure obtained using **VESTA** software after the final refinement of sample Sr_2SnO_4 is shown in the inset of Figure 3.4.

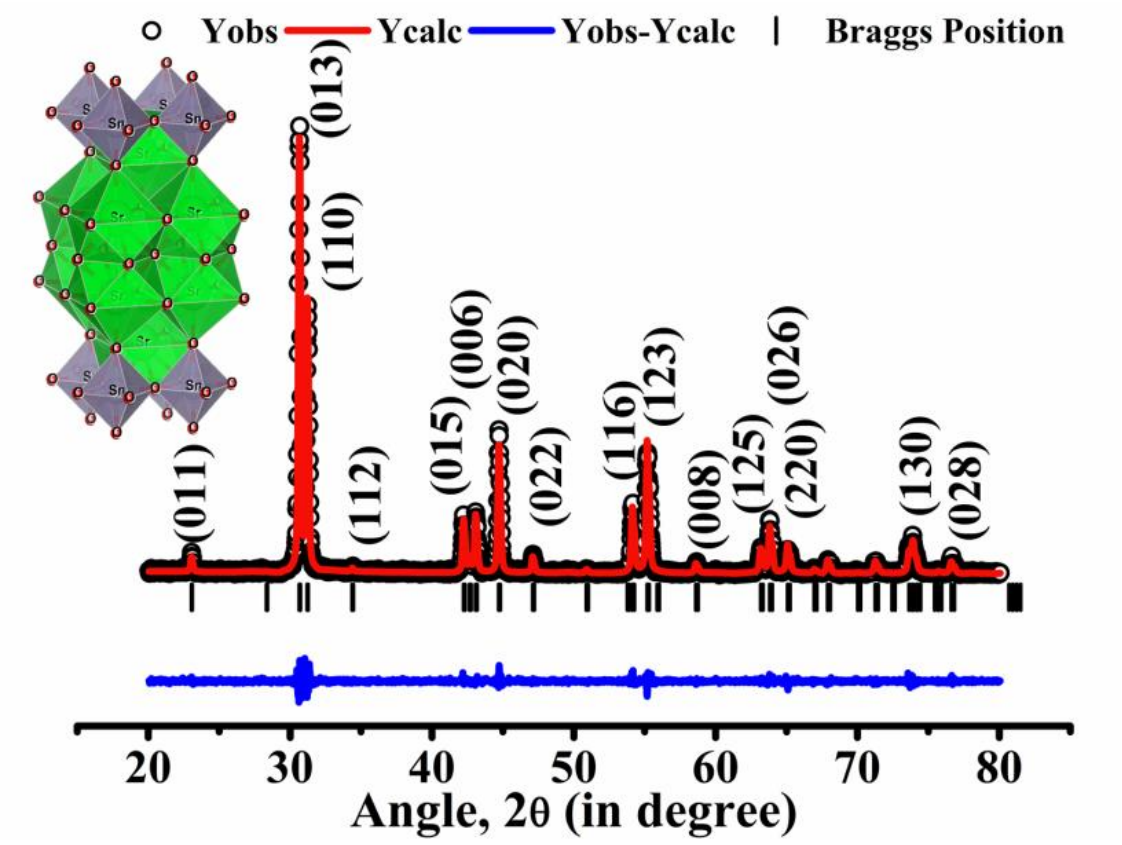

Figure 3.4 Rietveld refined pattern of X-ray diffraction data.

Table 3.1 Structural parameters, reliability factor, bond length, and bond angle of calcined powder of Sr_2SnO_4.

Crystal structure ---Tetragonal Space group ---- I4/mmm (139) Cell Volume -206.58 (Å)^3 Density - 5.68 gm/cm^3					
Atom	Site	x	y	Z	Occupancy
Sr	4e	0	0	0.35235	1.9956
Sn	2a	0	0	0	0.9985
O1	4e	0.5	0	0	2.7921
O2	4c	0	0	0.14860	1.1979
Selected Bond length (Å)			**Selected Bond angle (degree)**		
(Sr-O1) x 4	2.4567(4)		O2-Sr-O2	89.88	
(Sr-O2b) x 4	2.7464(3)		O1-Sn-O1	180.00	
(Sr-O2a) x 1	2.8672(5)		O1-Sr-O1	180.00	
(Sn-O1) x 4	2.0254(3)		O2-Sn-O1	90.00	
(Sn-O2) x 2	1.9835(4)		Sr-O2-Sn	87.43	
Sr-Sn	3.4124(4)		Sr-O1-Sr	84.96	
			Sr-O1-Sr	92.82	
Reliability parameters					
Rp	3.3				
Rwp	3.8				
Re	3.1				
S= R_{wp}/R_e	1.2				
χ^2	2.7				
R_{Bragg}	3.26				

3.2.3 Raman Spectrum analysis

Raman spectroscopy is more useful technique over diffraction methods. Low-concentration of impurity phases which cannot be detected by XRD could be observed by Raman spectroscopy. Furthermore, crystalline phases having different symmetries, with similar lattice parameters can distinguish more readily by Raman spectroscopy than diffraction methods [177]. Therefore, to study the structure of Sr_2SnO_4 in depth and detect impurity

phases, room temperature Raman spectrum has been recorded and shown in Figure 3.5. It is mentioned above that Sr_2SnO_4 crystallize in the tetragonal K_2NiF_4 structure under space group I4/mmm. According to group theory, materials having K_2NiF_4–type structure with I4/mmm space group has 14 optical modes ($2A_{1g} + 2E_g + 4A_{2u} + 5E_u + B_{2u}$) among which four modes ($2A_{1g} + 2E_g$) are only Raman active. Note that since the B atom occupies a Centro-symmetric site in the structure of A_2BO_4, therefore Raman active modes A_{1g} and E_g involve displacements of only A and O atoms [179].

Since no earlier records are available on the Raman spectrum of Sr_2SnO_4. Therefore, Raman spectrum of Sr_2SnO_4 has been compared with the spectrum of oxides having K_2NiF_4 type structure particularly with Sr_2TiO_4. Both Sr_2SnO_4 and Sr_2TiO_4 have similar structure and space group [180]. In the Raman spectrum of Sr_2TiO_4 an intense and broadband at 578 cm^{-1} was recorded corresponding to A_{1g} mode. However, this band is splitted into two bands: one at 561 cm^{-1} (ν_3) and another at 581 cm^{-1} (ν_3'). The splitting of the A_{1g} band in Sr_2SnO_4 is attributed to a large difference in the bond length of Sn–O in the layer and perpendicular to the layer (perpendicular to c-axis and parallel to c-axis). The values of these bond length are 2.02 and 1.91 Å for Sr_2SnO_4, whereas for Sr_2TiO_4 1.94 and 1.93 Å [181]. The two characteristics bands observed at 561 cm^{-1} and 581 cm^{-1} assigned as are attributed to the mode A_{1g} (TO—transverse optical phonon mode) and A_{1g} (LO— longitudinal optical phonon mode), respectively. The other bands (ν_1 and ν_1'), ν_2 and * are assigned to the E_u and A_{2u} and second order Raman bands of Sr_2SnO_4 respectively.

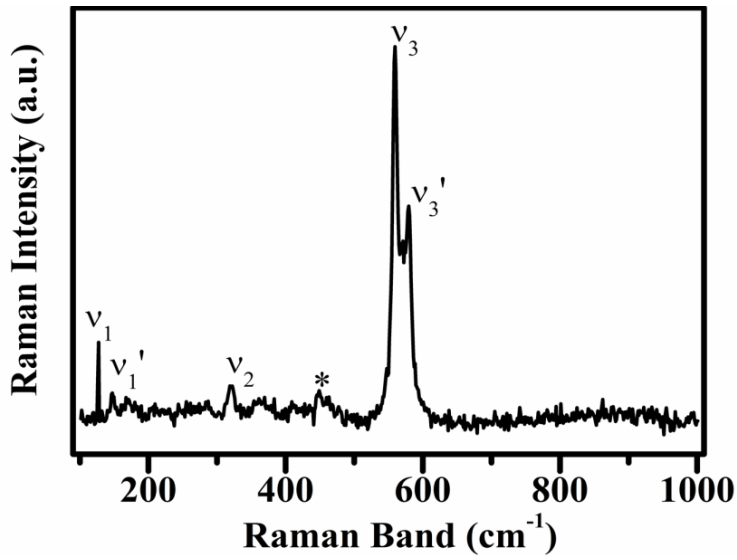

Figure 3.5 Room temperature Raman Spectrum of Sr_2SnO_4.

3.2.4 Fourier Transform Infrared Spectroscopy analysis

In order to analyze the presence of functional group present in the obtained sample, Fourier transformation Infra-red Spectroscopy has been carried out from wavenumber 400-1000 cm^{-1}. In the literature, it is reported that the FTIR spectrum of Sr_2SnO_4 contain two characteristic bands associated with vibrations Sr-O and SnO_6 which are observed at 502 cm^{-1} and 706 cm^{-1}, respectively [182]. Figure 3.6 depicts the room temperature Fourier transform infrared (FTIR) spectrum for the characteristics bands of Sr_2SnO_4, two characteristics bands observed at 512 and 706 cm^{-1} are associated with the vibrations of Sr-O and vibrations of Sn-O_6 which indicated the formation of single phase Sr_2SnO_4. Apart from these two characteristics band, two more bands observed at 856 cm^{-1}, and 950 cm^{-1} might be associated with vibration of $–CO_3$ adsorbed on the surface of powder during measurement.

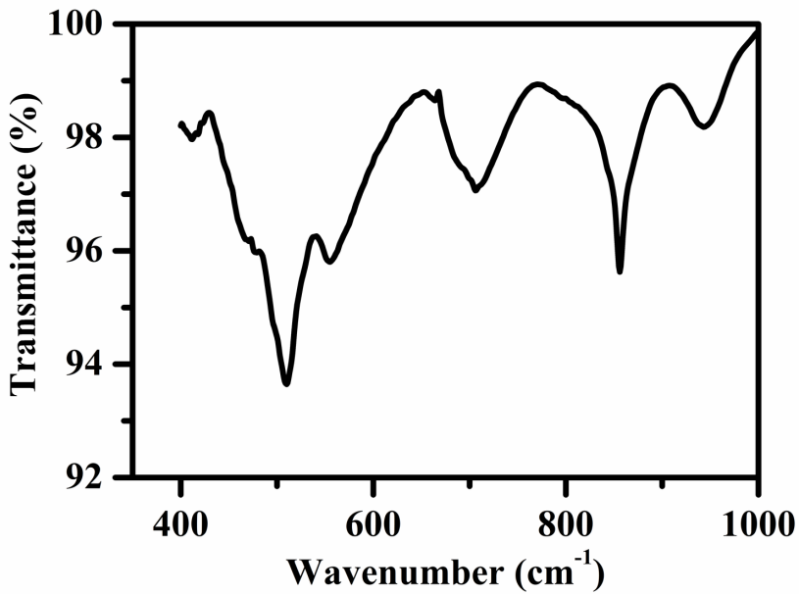

Figure 3.6 Fourier transform of Infra-red spectra of Sr_2SnO_4.

3.2.5 Microstructural study using FESEM

The microstructure of fractured surfaces of sintered pellet is shown in Figure 3.7(a). The grains are found to be uniformly distribution of spherical grains. The histogram for the spherical grains generated by "**Image J**" software is shown in Figure 3.7(b). To determine the average grain size, Gaussian function is fitted to the histogram. The average value of grain size determined by fitting is found to be (184 ± 20) nm.

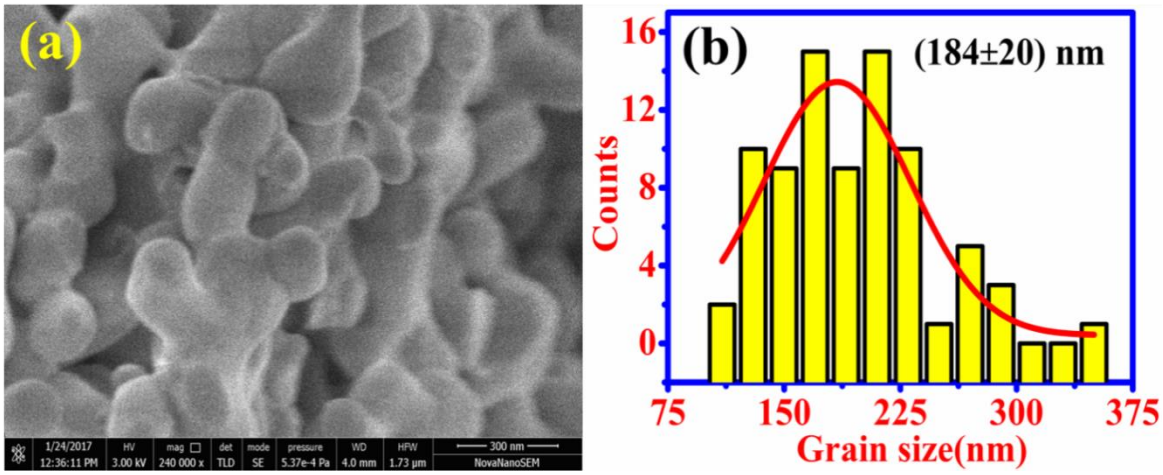

Figure 3.7 (a) SEM micrograph (b) Histogram generated for average grain.

3.2.6 X-ray Photoelectron Spectroscopy (XPS) analysis

The XPS survey scan spectrum for sample Sr_2SnO_4 is recorded and shown in Figure 3.8(a). The various peaks present in the survey scan report is assigned to elements, Sr(3d), Sn(5d) and O(1s) with the help of the literature [183]. The High Resolution X-ray Photoelectron Spectrum (HRXPS) of the individual elements, Sr(3d), Sn(5d) and O(1s) are shown in Figure 3.8(b), (c), (d) respectively. The core level peaks are fitted after the correction of background with Shirley function; the peak shape is modeled as Voigt, which is a mixed form of Lorentzian-Gaussian function. The position of peak is calibrated against the C(1s) correction, whose binding energy is observed at 284.6 eV [184]. The HRXPS of Sr (3d) shows the doublet peaks centered at 131.75 and 133.15 eV corresponding to the state $3d_{5/2}$ and $3d_{3/2}$. The observed peaks are well matched with Sr^{2+} state originated from Sr-O [185]. The HRXPS of Sn (5d) shows a doublet peaks centered at 485.45 and 493.85 eV assigned to $5d_{5/2}$ and $5d_{3/2}$ states of Sn, respectively. Both the peaks show an asymmetry in their peak shape towards lower binding energy side which might be indication of multivalency of Sn in the sample. In the literature, it is mentioned that Sn exists in both Sn^{4+} and $Sn2^{+}$ state in Sn-based perovskite oxides which are synthesized by high temperature solid state method. Therefore, the peak corresponding to $5d_{5/2}$ and $5d_{3/2}$ states are deconvoluted into two peaks centered at 484.82 and 493.22 eV of Sn^{2+} state and 484.95 and 493.35 eV of Sn^{4+} state [186]. On the other hand, HRXPS spectrum of O (1s) shows a single peak with slight asymmetry in peak shape towards higher binding energy side which indicates the presence of defects related oxygen. In order to identify the defect, the peak is deconvoluted and found two peaks centered at 529.57 and 530.35 eV. These peaks are assigned to the lattice oxygen and oxygen vacancies respectively of the sample using data available in the literature [46-48].

Thus XPS analysis indicated the presence of the defects Sn^{2+} and V_o^x in the synthesized samples. The neutral oxygen (V_o^x) vacancies may not be thermally stable and get

ionized singly ($V_o^{\bullet}$) and doubly ($V_o^{\bullet\bullet}$) charged. Further, the formation of oxygen vacancies in the samples takes place during sintering process of the sample. In this process oxygen leaves the lattice followed by a positively charge defect ($V_{\ddot{o}}$) can be understood by Eq. (1.10). This excess positive charge maintained by the reduction of multivalent ion Sn^{4+} according to the Eq. (3.5);

$$Sn^{4+} + 2e' \leftrightarrow Sn^{2+} \tag{3.5}$$

All the species are written in accordance with the Kronger-Vink notation of defect.

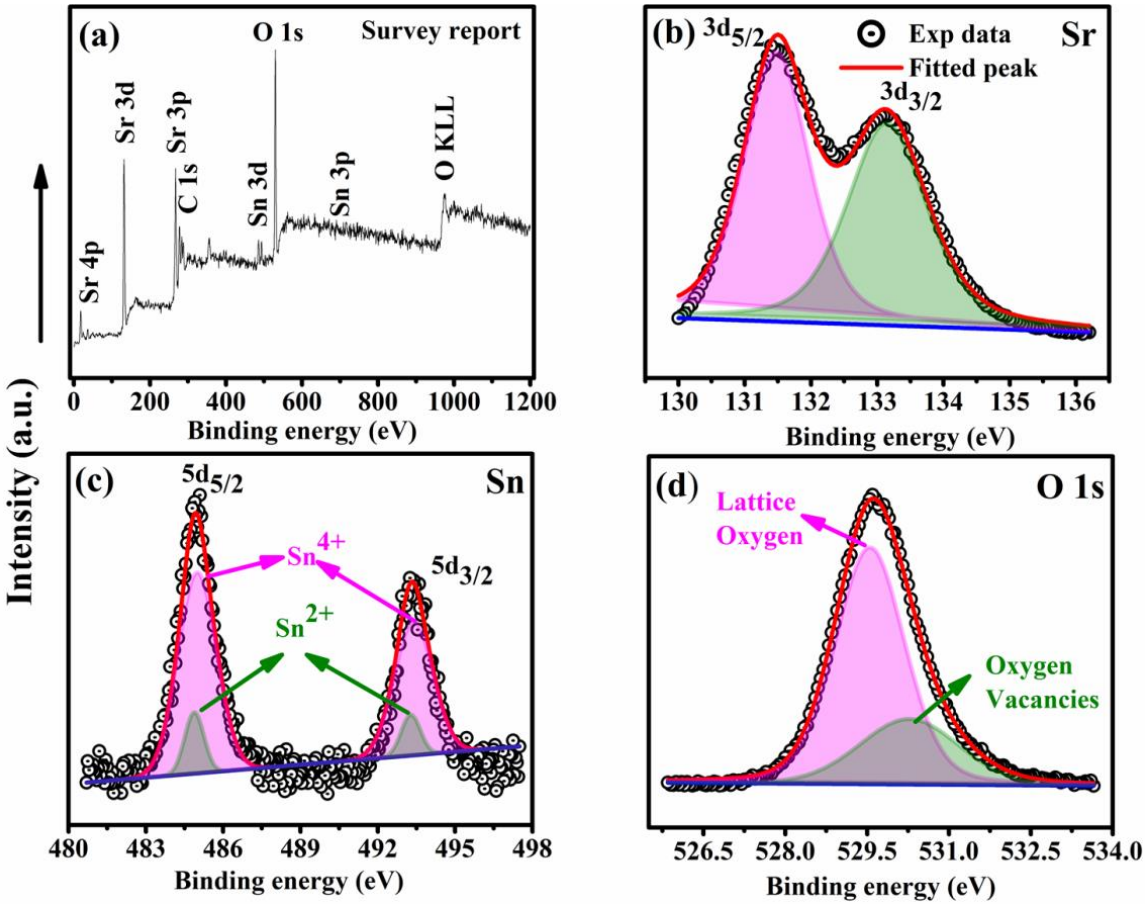

Figure 3.8 (a) Survey scan report of Sr_2SnO_4 (b-d) Core-level XPS spectra of individual element Sr (3d), Sn (5d) and O (1s).

3.2.7 UV-Visible Spectroscopy analysis

The Ultraviolet-visible (UV) spectroscopy measurement has been probed to investigate the optical absorbance of Sr_2SnO_4. The room temperature absorbance spectra of sample in the wavelength range 200-800 nm is shown in Figure 3.9. The band edge wavelength of the absorbance spectra has been determining from the extrapolation of the linear region on the x-axis where y=0, i.e., 290 nm. The band gap of the materials is defined as the gap present in between the top of lowest unoccupied molecular orbital (LUMO) to the bottom of highest occupied molecular orbital (HOMO). A formula $E_g = \frac{hc}{\lambda}$, is used to determine the band gap of Sr_2SnO_4 and found to be 4.60 eV. In order to determine the optical band gap more accurately, Tauc equation can be treated as a more reliable technique. The Tauc plot is generated by Eq. (2.21) and shown in Figure 3.9. The extrapolation of a linear region observed in Tauc plot to the X-axis gives the value of direct band gap i.e., 4.74 eV. By applying similar process for Indirect band gap which is defined as the transition mediated through the defect level present within the material is found to be 4.08 eV. The value of direct and indirect band gap for the Sr_2SnO_4 are reported to be 4.60 eV and 4.20 eV respectively [187]. The present value is slightly higher than the reported value, which might be ascribed to the lower crystallite size of Sr_2SnO_4 obtained in this investigation.

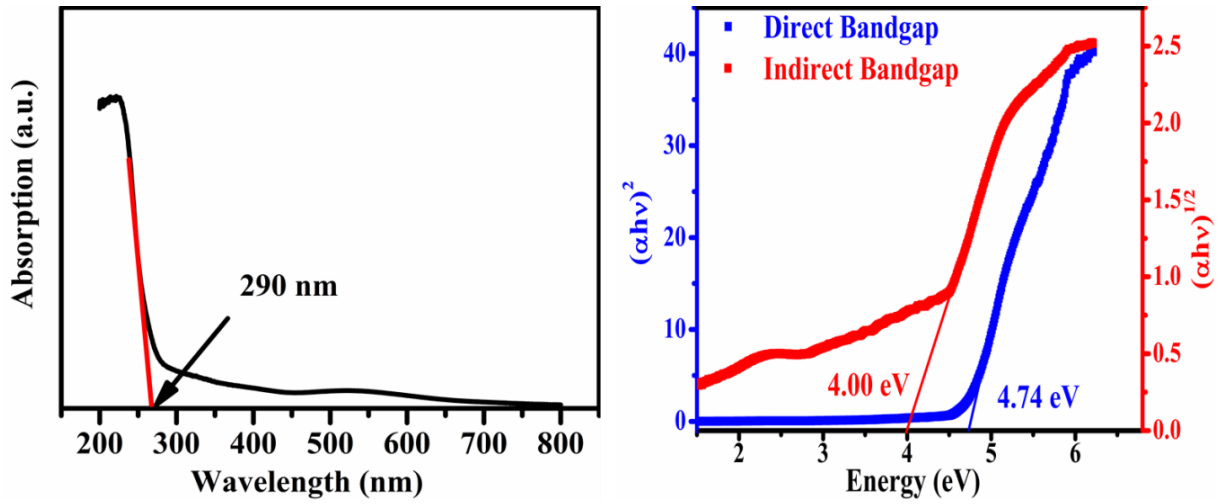

Figure 3.9 UV-Visible absorption spectra and Tauc plot of Sr_2SnO_4.

3.2.8 Electrical Characterization

3.2.8.1 Dielectric analysis

Variation of dielectric constant (ε_r) and dissipation factor (D) with temperature at four different frequencies are shown in Figure 3.10(a) and (b), respectively. Both dielectric constant and dissipation factor at a constant temperature decreases with increasing frequency. With increasing temperature, it is found that the dielectric constant and dissipation factor is increased at a particular frequency. Dielectric properties of a polycrystalline ceramic material are governed by the four types of polarization; electronic, ionic, orientational and space charge (Interfacial) polarization. These polarizations responds in different frequency ranges [188]. Interfacial polarization contributes at low frequencies ($\leq 10^3$ Hz) whereas orientation/dipolar polarisations in the frequency range 10^3 to 10^6 Hz. Other two polarizations (ionic and electronic) have their response above 10^6 Hz. At 1 KHz, the dielectric constant and dissipation factor were found to be highest this is because of the presence of all types of polarization. Sharp decrease in the value of dielectric constant and dissipation factor at 1 kHz suggests the major contribution of interfacial polarization in the sample. Interfacial polarization in a polycrystalline sample occurs either at inner dielectric boundary layers (at

interfaces of grain-grain boundary) on a microscopic scale, or at the external electrode-sample interface on a macroscopic scale. The dielectric constant and dissipation factor at 10 KHz are found to be almost constant, this may be because of the distance between the dipole is large and does not have enough energy to respond in presence of ac signal/thermal energy.

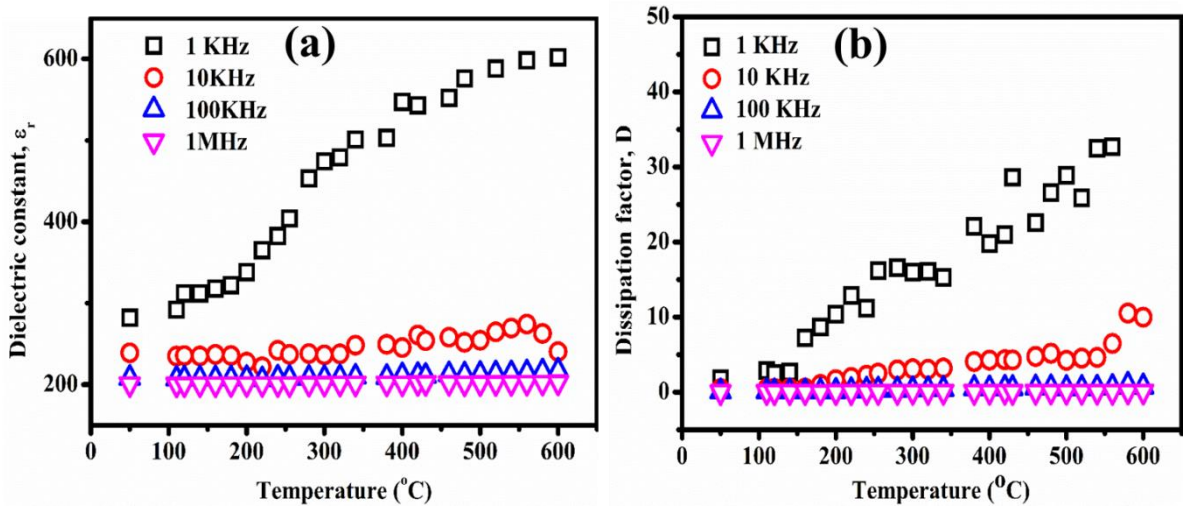

Figure 3.10 Variation of (a) Dielectric constant (b) Dissipation factor with temperature at different frequencies.

3.2.8.2 Modulus analysis

In order to get a deeper understanding of dielectric properties, electric modulus formalism has been used. In the complex plane electric modulus formalism, M^* is expressed in terms of complex dielectric constant (ε^*) as follow [189];

$$M^* = \frac{1}{\varepsilon^*} = \frac{1}{\varepsilon' + i\varepsilon''} \tag{3.6}$$

$$= \frac{\varepsilon'}{(\varepsilon' + \varepsilon'')^2} + i\frac{\varepsilon''}{(\varepsilon' + \varepsilon'')^2}$$

$$= M' + iM'' \tag{3.7}$$

Where ε' and ε'' are the real and imaginary parts of the dielectric constant and M' and M'' are the real and imaginary parts of the electric modulus.

The variation of real (M') parts of modulus against frequency at various temperatures are shown in Figure 3.11(a). At lower frequencies, the M'(f) approaches zero which suggest the negligible effect of polarization occurred at electrode-sample interface [189]. A dispersive region observed in the mid frequency region is related to conductivity relaxation process of the sample shifted towards higher frequency with increasing temperature while at higher frequency, M'(f) reaches to a asymptotic value that indicates the diminutive nature of forces, governing by the mobility of charge carriers under the action of an induced field. In order to study the relaxation process occurring in the sample, the imaginary part of modulus $M''(f)$ has been plotted as a function of frequency at different temperatures as shown in Figure 3.11(b). The imaginary part of modulus exhibits a well resolved peak at characteristic frequency (f_{max}). We observed that the peak position of characteristic frequency shifts towards higher frequency with increasing temperature. This indicates that the relaxation process is thermally activated. To understand the relaxation process, Bergman's approximation of Kohlrauch-Williams-Watts (KWW) function is employed to $M"$ data obtained in the frequency domain expressed as [189];

$$M^{"} = \frac{M^{"}{}_{max.}}{(1-\beta)+\frac{\beta}{1+\beta}\left[\beta\left(\frac{f_{max}}{f}\right)+\left(\frac{f}{f_{max}}\right)^{\beta}\right]} \qquad (3.8)$$

Where, $M^{"}{}_{max}$ is the maximum value of $M^{"}$, f_{max} is the frequency corresponding to $M^{"}{}_{max}$ and β is KWW parameter. The fitting of Eq. (3.8) to experimental data points of $M"(f)$ is shown by a solid line in Figure 3.11(b). From the fitting, the values of parameters f_{max}, $M^{"}{}_{max}$ and β at different temperatures are extracted. The variation of KWW parameter (β) with temperature is shown in Figure 3.11(c), the value of β remains almost 1 within the investigated temperature range. To identify the nature of the relaxation process occurring in the sample β is an important parameter to decide whether relaxation process is Debye type or Non-Debye type. If β is found to be unity, then the relaxation

process is Debye type while less than unity indicated the Non-Debye type relaxation process in the sample. In Non-Debye type relaxation, the materials should have a wide distribution of relaxation time. In present sample the value of β is almost 1 indicated the presence of Debye type relaxation process in sample.

In polycrystalline ceramic sample, the overall electrical properties have governed by the contribution of grains, grain boundaries and electrode. Each of these contributions is represented by a semicircle in Nyquist plot. The Nyquist plot obtained at 400^{o}C using modulus data (i.e. M'' vs. M') is shown in Figure 3.11(d). The Nyquist plot shows a single semicircle for present sample which is almost an ideal semicircle and their centre is lying on the axis real modulus M', which further confirms the presence of a single relaxation process in the sample i.e., Debye type relaxation. The intercept on real modulus (M') axis is equal to = $\frac{C_O}{C_{total}}$, and found to be in the order of 10^{-12} assigned to the contribution of bulk [156]. In order to understand the temperature dependent relaxation process involved in sample, the logarithmic of characteristic frequency (f_{max}) is plotted with respect to 1000/T and shown in Figure 3.11(e). Linear behavior of log f_{max} with 1000/T shows that relaxation process obeys Arrhenius relation which were given by

$$f_{max} = f_O \exp\left(-\frac{E_{relax.}}{k_B T}\right) \qquad (3.9)$$

Where, f_O is the relaxation time at infinite temperature, $E_{relax..}$ is the activation energy for relaxation process, k_B is Boltzmann's constant and T is absolute temperature. The linear fit of Eq. (3.9) to experimental data point has been used to estimate the activation energy of the sample. The activation energy E_{relax} is found to be (0.13±0.02) eV. The value of activation energy suggests that the relaxation process is occurring in the sample might be due to transfer of electron between the sites of Sn^{4+}/Sn^{2+} [159].

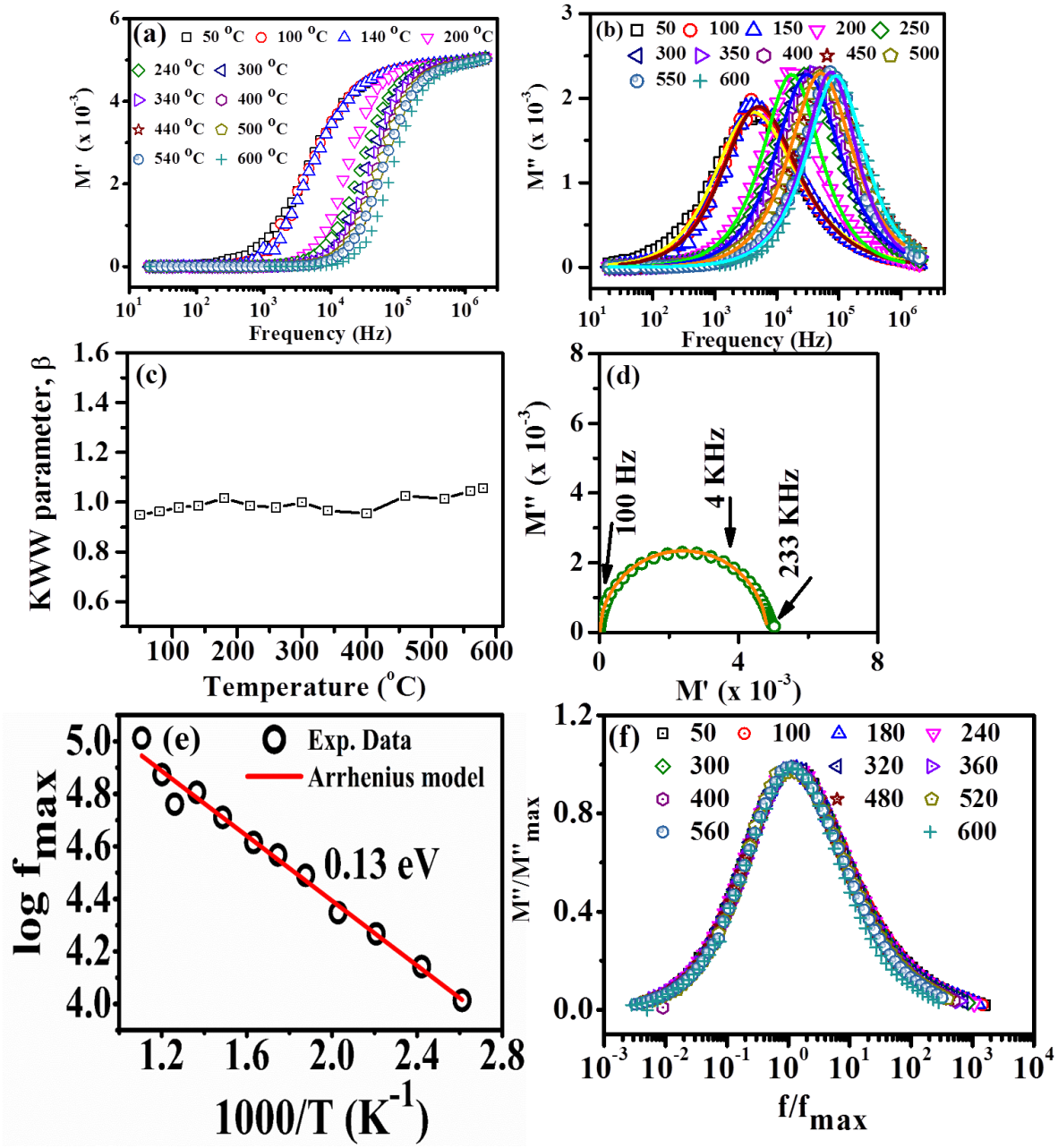

Figure 3.11 Variation of (a) Real part of modulus (M') (b) Imaginary part of modulus fitted with Eq. (3.9), with frequency at different temperatures. (c) KWW parameter with respect to temperature (d) Nyquist plot (e) Variation of $\log f_{max}$ with 1000/T (f) Scaled Modulus against scaled frequency at various temperatures.

Since the range of frequency and temperature is wide in this work, therefore possibility of changing in the relaxation mechanism can't be ruled out. Therefore, to study the temperature and frequency dependence on relaxation process the $M''(f)$ axis scaled by M_{max} and f- axis with f_{max} at different temperatures and shown in Figure 3.11(f). The overlapping of each

curve at different temperatures on a single master curve suggests that relaxation mechanism remains same for the sample at all temperature range.

3.2.8.3 AC conductivity analysis

In order to elucidate the conduction behaviour and correlate with the relaxation process as discussed above, the frequency dependent conductivity (σ_{ac}) of the sample measured at different temperatures are shown in Figure 3.12(a). The conductivity spectra clearly show two parts, one is parallel to frequency axis termed as dc conductivity (σ_{dc}) and second part is linearly increases with frequency termed as ac conductivity. In present case, the σ_{ac} follow universal Johnscher's power law similar to describe for other polycrystalline ceramics, glass ceramics and given by Eq. (2.36) [51-53].

The value of dc conductivity (σ_{dc}), power exponent (n) and hopping frequency (f_H) were obtained by fitting of Johnscher's power law to the experimental data points. The variation of dc conductivity with 1000/T is shown in Figure 3.12(b). A linear variation is observed between log σ_{dc} and 1000/ T confirms the Arrhenius type transport is operative in the sample and given by:

$$\sigma_{dc} = \sigma_o \exp\left(-\frac{E_{con.}}{k_B T}\right) \quad (3.10)$$

Where, σ_o is a constant, k_B is Boltzmann's constant and $E_{con.}$ is the activation energy for the dc conduction. The value of $E_{con.}$ is obtained by fitting of Eq. (3.10) to the dc conductivity data. The value of activation energy is found to be (0.16±0.02) eV. The obtained value of activation energy suggests that the conduction in the sample is take place by the hopping of electron between the sites of Sn^{2+}/Sn^{4+} [159]. Almost similar value of activation energy obtained from dc conductivity E_{cond} and characteristic frequency E_{relax} indicates that both the processes are governed by the same mechanism.

In the literature various mechanisms for ac conduction in crystalline and non-crystalline materials have been proposed. These models are based on the temperature and frequency dependence of power exponent n as mentioned below [189];

(i) Quantum mechanical tunnelling (QMT) of electrons predicts that power exponent s is dependence of frequency and independence of temperature.

(ii) Non-overlapping small-polaron tunneling (NSPT) model predicts an increase in s with an increase in temperature and frequency.

(iii) Overlapping large-polaron tunnelling (OLPT) model predicts that exponent s initially decreases with temperature; it attains a minimum value and again increases with temperature.

(iv) Hopping over Barrier (HOB) model predicts that the barrier height is not dependent on the inter-site separation; the value of frequency exponent s is predicted to be unity.

(v) Correlated Barrier Hopping (CBH) model predicts the value of s decreases with the increase of temperature.

The power exponent (n) of present sample with respect to temperature is shown in Figure 3.12(c). Since value of power exponent (n) for this sample remains independent of temperature, therefore Quantum Mechanical Tunnelling (QMT) model is the most suitable model to describe the ac conduction in the sample. According to Quantum Mechanical Tunnelling (QMT) model, frequency dependence of ac conductivity is given by Eq. (3.11) [191];

$$\sigma_{ac} = Ce^2 k_B T \alpha^{-1} [N(E_F)]^2 \omega {R_\omega}^4 \qquad (3.11)$$

Where, $N(E_F) =$ density of state at the Fermi level , R_ω is the distance tunnel by the electron at a frequency ω, α^{-1} is the attenuation length for single electron wave function, and τ_o is relaxation time at zero frequency. The variation of ac conductivity against temperature at 10

KHz is shown in Figure 3.12(d). By fitting of Eq. (3.11) to the experimental data of ac conductivity, the various parameters as given in Eq. (3.12) are determined. The value of α^{-1}, $N(E_F)$ and R_ω are found to be (1.37±0.02) x 10^{-8} cm, (1.67±0.01) x 10^{17} cm^{-3} and (4.45±0.05) Å respectively. The tunnelling distance (R_ω) is approximately equal to the distance between the two consecutive Sn sites along a and b axis. This result supports the hypothesis of conduction via transfer of electron from Sn^{2+} to Sn^{4+} site through thermal assisted quantum mechanical tunnelling process [192].

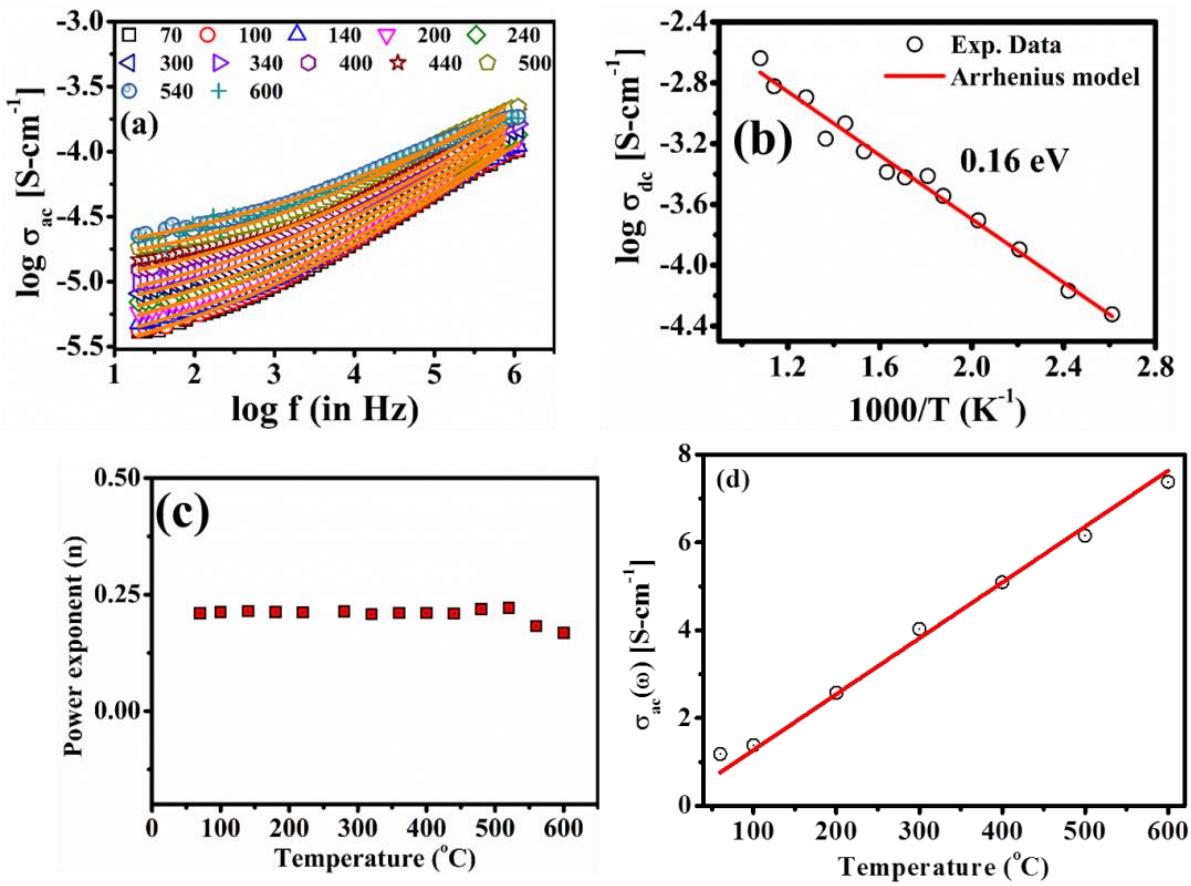

Figure 3.12 (a) Logarithmic conductivity with logarithmic frequency (fitted with power law) (b) Arrhenius plot (c) Power exponent (n) with temperature (d) logarithmic of ac conductivity with the temperature at a constant frequency (10 KHz).

In order to study temperature and frequency dependency on conduction mechanism of the sample, Ghosh scaling is applied [193]. For this, the ac conductivity data is scaled

by $\log\left(\frac{\sigma}{\sigma_{dc}}\right)$, and frequency as $\log\left(\frac{f}{f_H}\right)$ and plotted in Figure 3.13. The scaled conductivity obtained at different temperatures was superimposed on a single master curve which suggests that the source of conduction at different temperatures follows a similar mechanism.

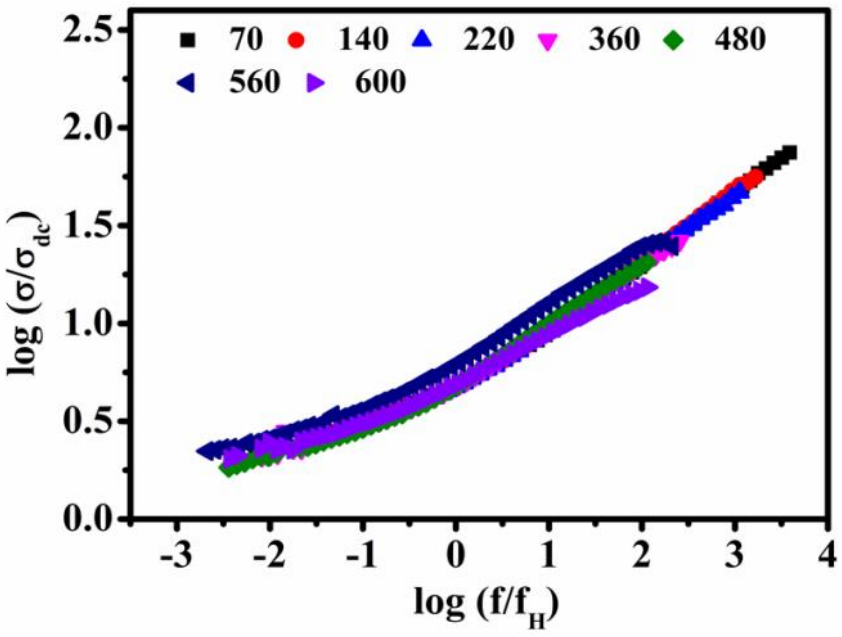

Figure 3.13 Scaled conductivity vs. scaled frequency spectrum at different temperatures.

3.3 Conclusions

Ruddlesden Popper oxide phase Sr_2SnO_4 synthesized in this work has a tetragonal structure with space group I4/mmm, lattice parameters a=b=(4.05084±0.00005)Å, c=(12.59040±0.00002)Å. Further, the obtained powder is characterized using various experimental techniques like Raman, FTIR, and UV-Vis absorption to study their structure and phase. The electrical properties of ceramic are studied as a function of frequency and temperature. The dielectric constant and dissipation factor is found to be almost independent of temperature > 1 KHz. A single Debye type relaxation process is observed in the sample. The ac conductivity spectra follow universal Johnscher's power law. Almost same value of the activation energy obtained for relaxation (E_{relax}) and conduction(E_{cond}) confirms that dielectric relaxation and conduction have the same origin. It is proposed that the relaxation

and conduction are taking place via thermally assisted Quantum Mechanical Tunnelling of electrons from Sn^{2+} sites to Sn^{4+} sites. Stable value of dielectric constant and lower value of dissipation factor makes it a potential candidate for thermal stable capacitor application.